

Hemodynamic Deconvolution Demystified: from Paradigm Free Mapping to Total Activation

Eneko Uruñuela^{a,b,*}, Thomas A.W. Bolton^{c,d}, Younes Farouj^d, Dimitri Van de Ville^{d,e}, César Caballero-Gaudes^a

^a*Basque Center on Cognition, Brain and Language (BCBL), Donostia-San Sebastián, Spain.*

^b*University of the Basque Country (EHU/UPV), Donostia-San Sebastián, Spain.*

^c*Gamma Knife Center, Department of Clinical Neuroscience, Centre Hospitalier Universitaire Vaudois (CHUV), Lausanne, Switzerland*

^d*Swiss Federal Institute of Technology Lausanne (EPFL), Lausanne, Switzerland.*

^e*Faculty of Medicine of the University of Geneva, Geneva, Switzerland*

Abstract

Deconvolution of the hemodynamic response is an important step to access short timescales of brain activity recorded by fMRI. Albeit conventional deconvolution algorithms have been around for a long time (e.g., Wiener deconvolution), recent state-of-the-art methods based on sparsity-pursuing regularization are attracting increasing interest to investigate brain dynamics. This technical note revisits the main concepts underlying two main methods, Paradigm Free Mapping and Total Activation, in the most accessible way. Despite their apparent differences, these methods are theoretically equivalent as they represent the synthesis and analysis sides of the same problem. We demonstrate this equivalence in practice with their best-available implementations using both simulations, with different signal-to-noise ratios, and experimental data of motor task and resting-state fMRI. We evaluate the parameter settings that lead to equivalent results, and benchmark the computational speed of both algorithms. This note is useful for practitioners interested to better understand state-of-the-art hemodynamic deconvolution, and want to make use of the most efficient implementation.

Keywords: fMRI deconvolution, paradigm free mapping, total activation

1. Introduction

Functional magnetic resonance imaging (fMRI) data analysis is often directed to disentangling and understanding the neural processes that occur among brain regions. While interactions in the brain are electrical in nature, the blood oxygenation level-dependent (BOLD) signal present in fMRI data reflects hemodynamics. Thus, an intermediate step that estimates the underlying neuronal activity from the BOLD signal can prove to be useful for understanding such interactions. Often, the analysis of task fMRI data relies on general linear models (GLM) to detect maps of brain activity by using the information about the timings of the BOLD events. However, this information can be unknown, inaccurate, or insufficient in some scenarios. In such cases, and given the nature

*Corresponding author

Email address: e.urunuela@bcbl.eu (Eneko Uruñuela)

10 of the BOLD signal, the appropriate approximation of the neuronal activity can be obtained by means of deconvolution with an assumed hemodynamic response (Gitelman et al. 2003).

15 Deconvolution and methods alike are becoming more popular for exploring time-varying activity in fMRI data within a number of neuroimaging studies due to their potential to blindly disentangle neural dynamics. One of such cases is the study of resting-state fluctuations with the aim of gaining insight into the origin of the signals driving functional connectivity and its temporal dynamics, as well as the organizational principles of brain function; i.e., to study and deconstruct the spatio-temporal structure of functional components that dynamically construct resting-state networks (Karahanoglu and Van De Ville 2015; ; Kinany et al. 2020; Gonzalez-Castillo et al. 2019; Allan et al. 2015). Deconvolution techniques can also prove to be helpful in clinical conditions 20 to characterize functional alterations of patients with a progressive stage of multiple sclerosis at rest (Bommarito et al. 2020), to find functional signatures of prodromal psychotic symptoms and anxiety at rest on patients suffering from schizophrenia (Zöller et al. 2019), to detect the foci of interictal events in epilepsy patients without an EEG recording (Lopes et al. 2012), or to study functional dissociations observed during non-rapid eye movement sleep that are associated with 25 reduced consolidation of information and impaired consciousness (Tarun et al. 2020).

30 A series of recent studies have also attempted to understand neural processes by studying the interactions between BOLD responses without estimating the underlying neuronal activity. For instance, co-activation patterns have been used to replicate seed correlation-based resting-state functional networks with a small portion of the data (Liu and Duyn 2013; Liu et al. 2013, 2018; Majeed et al. 2009, 2011; Cifre et al. 2020a,b; Zhang et al. 2020). Likewise, the dynamics of 35 functional connectivity have recently been investigated with the use of co-fluctuations and edge-centric techniques on tasks (Faskowitz et al. 2021), resting-state (Esfahlani et al. 2020) and naturalistic paradigms (Faskowitz et al. 2020; Betzel et al. 2020). Methods based on the multiplication of temporal derivatives have also been presented for the estimation of dynamic functional connectivity on task fMRI data (Shine et al. 2015, 2016).

40 This note revisits synthesis- and analysis-based deconvolution methods for fMRI data and comprises four sections. In the first, we present the theory behind two state-of-the-art deconvolution approaches based on estimators that promote sparsity: Paradigm Free Mapping (PFM) (Cabantuero Gaudes et al. 2013) — available as *3dPFM* and *3dMEPFM* in AFNI — and Total Activation (TA) (?) — available as part of the *iCAPs toolbox*. We then assess their performance controlling for a fair comparison on simulated and experimental data. Finally, we discuss the benefits and shortcomings of the techniques and conclude with our vision on potential extensions and developments.

2. Theory

The hemodynamic response to neuronal activity can be modeled as the convolution the activity-inducing signal $s(t)$ with the hemodynamic response function $h(t)$ as $x(t) = h(t) * s(t)$ (Gitelman et al. 2003). Then, the fMRI signal at a given voxel $y(t)$ can be decomposed into neuronal-related hemodynamic $x(t)$ and noise components $n(t)$ as:

$$y(t) = x(t) + n(t). \quad (1)$$

The maximum likelihood estimate of the hemodynamic response to the underlying neural activity can be calculated using the ordinary least-squares estimator that minimizes the residual sum of squares between the modeled (\mathbf{X}) and measured (\mathbf{y}) signals. In conventional fMRI data analysis,

when the information about the timings of the BOLD events is known, the activity inducing signal, also known as the stimulus function of a condition of interest, is retrieved by solving a general linear model (GLM) problem such that:

$$\mathbf{y} = \mathbf{X}\beta + \mathbf{n}, \quad (2)$$

where the measured signal (\mathbf{y}) is described as the sum of one or more experimental design variables (\mathbf{X}), each multiplied by a weighting factor (β). The signal model in (1) can also be extended to represent the neuronal signal \mathbf{s} in terms of its innovation signal \mathbf{u} , i.e., its derivative, as $\mathbf{s} = \mathbf{L}\mathbf{u}$ where $\mathbf{L} \in \mathbb{R}^{N \times N}$ is an integration operator (Cherkaoui et al. 2019; Uruñuela et al. 2020). Thus, the GLM problem in (2) can be rewritten as $\mathbf{y} = \mathbf{XL}\beta + \mathbf{n}$ to detect changes that drive the neuronal signal.

Yet, when the information about the timings of the BOLD events is unavailable, the design matrix \mathbf{X} has to be described as the Toeplitz convolution matrix with shifted HRFs (see Figure 3B). In this case, the estimates of the neuronal activity \mathbf{s} must be constrained with a regularization term to attenuate the collinearity and high variability of the new design matrix \mathbf{H} , and the estimation of the underlying neural activity becomes a deconvolution problem such that:

$$\mathbf{y} = \mathbf{H}\mathbf{s} + \mathbf{n}, \quad (3)$$

where $\mathbf{y}, \mathbf{s} \in \mathbb{R}^N$, $\mathbf{H} \in \mathbb{R}^{N \times N}$ is the HRF in Toeplitz matrix form, and N is the number of frames of the fMRI acquisition.

2.1. Synthesis-based deconvolution

Synthesis-based deconvolution models are those in which the candidate estimator is synthesized (i.e. constructed) from a linear combination of dictionary atoms. Paradigm Free Mapping (PFM) is based on such construction as its estimator \mathbf{H} is described by shifted HRFs (atoms). Hence, considering the signal model introduced in (1); i.e., the BOLD signal (\mathbf{x}) is the result of convolving the underlying neural activity (\mathbf{s}) with the hemodynamic response (\mathbf{H}), the activity-inducing signal can be estimated by solving the following regularized least-squares problem (Gaudes et al. 2011; Caballero Gaudes et al. 2013; Uruñuela et al. 2020):

$$\hat{\mathbf{s}} = \arg \min_{\mathbf{s}} \frac{1}{2} \|\mathbf{y} - \mathbf{H}\mathbf{s}\|_2^2 + \Omega(\mathbf{s}), \quad (4)$$

where $\Omega(\mathbf{s})$ is the regularization term.

Assuming that single-trial BOLD responses are the result of brief bursts of neuronal activation, the activity-inducing signal \mathbf{s} must be a sparse vector. Thus, sparse estimates of \mathbf{s} could be obtained by substituting $\Omega(\mathbf{s})$ in (5) with an l_0 -norm and solving the optimization problem (Bruckstein et al. 2009). However, due to the convolution model defined in (5), finding the optimal solution to the problem demands an exhaustive search across all possible combinations of the columns of the design matrix \mathbf{H} . Hence, a pragmatic solution is to solve the optimization problem with the use of an l_1 -norm, or LASSO (Tibshirani 1996), which is a convex function and therefore provides fast convergence to the optimal solution.

$$\hat{\mathbf{s}} = \arg \min_{\mathbf{s}} \frac{1}{2} \|\mathbf{y} - \mathbf{H}\mathbf{s}\|_2^2 + \lambda \|\mathbf{s}\|_1, \quad (5)$$

where λ regulates how sparse the optimal solution is.

Such formulation provides flexibility to expand the capabilities of PFM. For instance, incorporating the integration operator \mathbf{L} into the design matrix \mathbf{H} allows the recovery of the innovation signal \mathbf{u} ; i.e., the derivative of the activity-inducing signal \mathbf{s} . Therefore, the innovation signal can be estimated by solving the following optimization problem (Cherkaoui et al. 2019; Uruñuela et al. 2020):

$$\hat{\mathbf{u}} = \arg \min_{\mathbf{u}} \frac{1}{2} \|\mathbf{y} - \mathbf{H}\mathbf{L}\mathbf{u}\|_2^2 + \lambda \|\mathbf{u}\|_1. \quad (6)$$

2.2. Analysis-based deconvolution

On the other hand, the estimator of the signal is analyzed in analysis-based deconvolution models, i.e., some aspects of it are calculated and penalized during the estimation process. For instance, Total Activation (TA) proposes to use a linear differential operator L_h that inverts the hemodynamic system based on activelets to recover the activity-inducing signal \mathbf{s} (?Khalidov et al. 2011; Karahanoglu et al. 2011):

$$L_h\{x\}(t) = s(t) \quad (7)$$

where x is the neuronal-related signal; i.e., the activity inducing signal \mathbf{s} convolved with the HRF, and L_h is defined as

$$L_h = \prod_{i=1}^{M_1} (D - \alpha_i I) \left(\prod_{j=1}^{M_2} (D - \gamma_j I) \right)^{-1}, \quad (8)$$

where D is the derivative operator, $\alpha_i (i = 1, \dots, M_1)$ define the zeros of the filter, $\gamma_j (j = 1, \dots, M_2)$ represent the poles, I is the identity matrix and $M_1 > M_2$. Given the relationship between the activity-inducing and the innovation signal, the latter can be recovered as:

$$L\{x\}(t) = D\{s\}(t) = u(t) \quad (9)$$

where $L = DL_h$ and D is the derivative.

Therefore, for a given voxel, the neuronal-related signal could be estimated by solving the following regularized least-squares problem:

$$\hat{\mathbf{x}} = \arg \min_{\mathbf{x}} \frac{1}{2} \|\mathbf{y} - \mathbf{x}\|_2^2 + \Omega(\mathbf{x}), \quad (10)$$

where \mathbf{y} is the fMRI data and $\Omega(\mathbf{x})$ is the following l_1 -norm regularization term:

$$\hat{\mathbf{x}} = \arg \min_{\mathbf{x}} \frac{1}{2} \|\mathbf{y} - \mathbf{x}\|_2^2 + \lambda \|\Delta_L \{\mathbf{x}\}\|_1, \quad (11)$$

where λ is the regularization parameter.

This work evaluates the core of the two techniques, i.e., the regularized least-squares problem with temporal regularization, which corresponds to the generalized total-variation operator in Total Activation. Therefore, we do not study the impact of spatial constraints, as we assume that spatial regularization terms should perform identically on both methods.

2.3. Selection of the regularization parameter

The correct selection of the regularization parameter λ is a critical decision for the accurate performance of deconvolution methods. Even though many techniques have been proposed in the literature, the optimal strategy that selects λ is yet to be found. Algorithms like least angle regression (LARS) (Efron et al. 2004) provide all the possible solutions to the optimization problem and their corresponding value of λ , i.e., the regularization path, but don't provide the optimal solution. Therefore, strategies that exploit the regularization path can provide a selection of λ that is close to the optimal. For instance, in Paradigm Free Mapping, the optimal result is given by the Bayesian Information Criterion (BIC) (Schwarz 1978), i.e., the regularization path solution with the minimum BIC is considered optimal. Another approach could be to update the regularization parameter λ on every iteration n like Total Activation does, so that the residuals converge to a previously estimated noise level of the data fit $\tilde{\sigma}$. The pre-estimated noise level is calculated from the median absolute deviation of fine-scale wavelet coefficients (Daubechies, order 3) (?):

$$\lambda^{n+1} = \frac{N\tilde{\sigma}}{\frac{1}{2}\|\mathbf{y} - \mathbf{x}^n\|_F^2} \lambda^n. \quad (12)$$

Here, we compare the performance of the two deconvolution algorithms with both selection criteria and in terms of the estimation of the activity-inducing signal \mathbf{s} using the *spike model* in (5) and the innovation signal \mathbf{u} using the *block model* in (6).

3. Methods

3.1. Simulated data

In order to compare the two methods while controlling for their correct performance, we simulated a 400 seconds (TR = 2 s) activity-inducing signal with five neuronal events, convolved it with the canonical HRF, and we added noise of different sources (physiological, thermal, and motion-related) with different signal-to-noise ratios (SNR = [20 dB, 10 dB, 3 dB]) that represent low, medium and high levels of noise as shown in Figure 1. Noise was created following the procedure in (Caballero Gaudes et al. 2013) as the sum of uncorrelated Gaussian noise and sinusoidal signals to simulate a realistic noise model with thermal noise, cardiac and respiratory physiological fluctuations. We generated the sinusoidal term as

$$\sum_{i=1}^2 \frac{1}{2^{i-1}} (\sin(2\pi f_{r,i}t + \phi_{r,i}) + \sin(2\pi f_{c,i}t + \phi_{c,i})), \quad (13)$$

with up to second-order harmonics per cardiac ($f_{c,i}$) and respiratory ($f_{r,i}$) component that were randomly generated following normal distributions with variance 0.04 and mean if_r and if_c , for $i = [1, 2]$. We set the fundamental frequencies to $f_r = 0.3$ Hz for the respiratory component (Birn et al. 2006) and $f_c = 1.1$ Hz for the cardiac component (Shmueli et al. 2007). The phases of each harmonic ϕ were randomly selected from a uniform distribution between 0 and 2π radians. In order to simulate physiological noise that is proportional to the change in BOLD signal, a variable ratio between the physiological (σ_P) and the thermal (σ_0) noise was modeled as $\sigma_P/\sigma_0 = a(tSNR)^b + c$, where $a = 5.01 \times 10^{-6}$, $b = 2.81$, and $c = 0.397$. The physiological-thermal noise model was extracted following the experimental measures of the physiological-to-thermal noise ratio at 7T in Table 3 in (Triantafyllou et al. 2005). The code used to simulate the data can be found in the GitHub repository shared in section 6.

80 *3.2. Experimental data*

Motor task dataset: One healthy subject was scanned in a 3T MR scanner (Siemens) as part of a larger experiment under a Basque Center on Cognition, Brain and Language Review Board-approved protocol. T2*-weighted multi-echo fMRI data was acquired with a multiband (MB) multi-echo gradient echo-planar imaging sequence (340 scans, 52 slices, Partial-Fourier = 6/8, voxel size = 2.4x2.4x3 mm³, TR = 1.5 s, TEs = 10.6/28.69/46.78/64.87/82.96 ms, multiband factor = 4, flip angle = 70°, GRAPPA = 2).

85 During the fMRI acquisition, subjects performed a motor task consisting of five different movements (left-hand finger tapping, right-hand finger tapping, moving the left toes, moving the right toes and moving the tongue). These conditions were randomly intermixed every 16 seconds, and
90 were only repeated once the entire set of stimuli were presented. Data preprocessing consisted of optimally combining the echo time datasets, detrending of up to 5th-order Legendre polynomials, spatial smoothing (3 mm FWHM) and normalization to signal percentage change. Figure 2 shows the time-series of a representative voxel in the motor cortex, where the colored bands illustrate the onset and duration of the right-hand finger-tapping condition of the paradigm.

95 **Resting-state datasets:** One healthy subject was scanned in a 3T MR scanner (Siemens) as part of a larger experiment under a Basque Center on Cognition, Brain and Language Review Board-approved protocol. Two runs of T2*-weighted fMRI data were acquired during resting-state, each with 10 min duration, with 1) a standard gradient-echo echo-planar imaging sequence (monoband) (TR = 2000 ms, TE = 29 ms, flip-angle = 78°, matrix size = 64x64, voxel size = 3x3x3 mm³, 33 axial
100 slices with interleaved acquisition, slice gap = 0.6 mm) and 2) a simultaneous multislice gradient-echo echo-planar imaging sequence (multiband factor = 3) developed by the Center of Magnetic Resonance Research (University of Minnesota, USA; TR = 800 ms, TE = 29 ms, flip-angle = 60°, matrix size = 64×64, voxel size = 3x3x3 mm³, 42 axial slices with interleaved acquisition, no slice gap). Single-band reference images were also collected in both resting-state acquisitions for head
105 motion realignment. Field maps were also obtained to correct for field distortions.

110 During both acquisitions, participants were instructed to keep their eyes open, fixating a white cross that they saw through a mirror located on the head coil, and not think about anything specific. The data was pre-processed using AFNI (Cox 1996). First, volumes corresponding to the initial 10 seconds were removed to allow for a steady-state magnetization. Then, the voxel time-series were
115 despiked to reduce large-amplitude deviations and slice-time corrected. Inhomogeneities caused by magnetic susceptibility were corrected with FUGUE (FSL) using the field map images (Jenkinson et al. 2012). Next, functional images were realigned to a base volume (monoband: volume with the lowest head motion; multiband: single-band reference image). Finally, a simultaneous nuisance regression step was performed comprising up to 6th-order Legendre polynomials, low-pass filtering
120 with a cutoff frequency of 0.25 Hz (only on multiband data to match the frequency content of the monoband), 6 realignment parameters plus temporal derivatives, 5 principal components of white matter (WM), 5 principal components of lateral ventricle voxels (anatomical CompCor) and 5 principal components of the brain's edge voxels. WM, CSF and brain's edge-voxel masks were obtained from Freesurfer tissue and brain segmentations. In addition, scans with potential artifacts were identified and censored as the euclidean norm of the temporal derivative of the realignment parameters (ENORM) was larger than 0.4, and the proportion of voxels adjusted in the despiking step exceeded 10%.

3.3. Selection of the hemodynamic response function

With the aim of making a fair comparison of the two methods, we first compared their hemodynamic response functions. Figure 3A shows the difference in the hemodynamic response function that PFM and TA use by default for TR = 0.1 s and TR = 1 s adjusted to peak amplitude of one; i.e., the canonical HRF and the HRF resulting from the linear differential operator. The most observable difference between the two HRFs is the time to peak: the HRF used by Total Activation does not begin at zero while the one used by PFM does.

While Paradigm Free Mapping allows for the use of any hemodynamic response function — the columns of the design matrix \mathbf{H} are composed by shifted versions of the HRF — the linear differential operator in TA is tailored for a fixed HRF. Hence, for practical reasons, we reproduced the HRF in the Total Activation filter and incorporated it into the PFM formulation (Figure 3B).

4. Results

4.1. Selection of the regularization parameter based on the estimation of the noise

We calculated the regularization path with PFM (as described in 4.2) and selected the λ corresponding to the residuals that were closest to the estimated noise level of the data. We applied Total Activation with temporal regularization in its original form. Figure 4B depicts the estimated activity-inducing, innovation, and activity-related signals when updating λ following (12) in the three simulated SNR settings using the spike model (left) and the block model (right). Figure 4B (left) shows nearly identical results between PFM (left) and TA (right) with the use of the spike model. The minimal differences are the result of slight dissimilarities in the convergence of the residuals to the estimated noise level of the data. Likewise, the use of the block model with a selection of λ based on the MAD estimate of the noise yields results that are identical in practice as shown in Figure 4B (right).

4.2. Selection of the regularization parameter by solving the regularization path

Paradigm Free Mapping bases its selection of the regularization parameter on the BIC. Hence, we calculated the regularization path with PFM by means of the least angle regression (LARS) algorithm (Efron et al. 2004) and used the λ s from the regularization path to solve the deconvolution problem with Total Activation.

Figure 4A (left) shows the regularization paths of PFM and TA side by side for the three SNR conditions for the spike model; i.e., the inverse problem described in (5). Each iteration of LARS reduces the value of λ ; i.e., reduces the sparsity promoted by the l_1 -norm, and reveals new non-zero coefficients as shown in the x-axis of the heatmaps. Vertical black lines depict the selection of the regularization parameter based on BIC, and thus, the colored coefficients indicated by the vertical lines depict the estimated activity-inducing signal $s(t)$. Figure 4A (right) illustrates the resulting estimation of the activity-inducing and neuronal-related signals when basing the selection of λ on BIC for the three simulated SNR conditions. Given that the regularization paths of both techniques are identical, the BIC-based selection of the regularization parameter and the results of deconvolving with said λ are identical too (see Figure ??). Thus, Figure 4A demonstrates that, regardless of the simulated SNR condition, both deconvolution algorithms produce identical regularization paths when the same HRF and regularization parameters are applied, and hence, identical estimates of the activity-inducing signal s and neuronal-related signal x .

The regularization path to estimate innovation signals yields mainly undistinguishable results for both PFM and TA methods as shown in Figure 4A (left). Again, the BIC-based selection

of λ is identical for both PFM and TA, and the estimation of the innovation signal \mathbf{u} shows no distinguishable differences between the algorithms (see Figure 4A right). Therefore, both Paradigm Free Mapping and Total Activation yield nearly identical regularization paths and estimates of the innovation signal regardless of the simulated SNR condition when applying the same HRF and regularization parameters with the block model.

170

4.3. Performance on experimental data

Additionally, in order to describe the extent of the discrepancies between the techniques, we calculated the residual sum of squares (RSS); i.e., the sum of squares of the differences between the estimated activity-inducing or innovation signals of PFM and TA as:

$$RSS = \frac{\sum (\hat{s}_{PFM} - \hat{s}_{TA})^2}{N}, \quad (14)$$

where N is the number of frames of the acquisition.

Figure 5 depicts the RSS of the spike (Figure 5A) and block (Figure 5B) models for the three experimental datasets introduced: i.e., motor, monoband and multiband. It is clear that RSS values are lower than those of the activity-inducing and innovation signals, suggesting that the differences between Paradigm Free Mapping and Total Activation are negligible. Furthermore, the largest differences can be seen in regions with high vasculature and are probably a result of differences in the amplitude of the estimated activity-inducing and innovation signals.

175

5. Discussion

This work demonstrates that Paradigm Free Mapping and Total Activation yield practically identical results when the same HRF model and regularization parameter are employed, demonstrating that synthesis and analysis models are equivalent for temporal fMRI deconvolution. Thus, previously observed differences in performance must be due to differences in usage options. With the equivalence in the temporal deconvolution demonstrated, it is reasonable to assume that additional regularization terms in the spatial or temporal domains would not modify this equivalence when convex operators are employed; e.g., when the regularization problem can be solved by means of the Fast Iterative Shrinkage-Thresholding Algorithm (FISTA) (Beck and Teboulle 2009) or the Generalized Forward-Backward Splitting (Raguet et al. 2013) techniques. Our findings are in line with the equivalence of analysis and synthesis methods in under-determined cases ($N \leq V$) as demonstrated in (Elad et al. 2007).

180

Taking into account the advantages and disadvantages of the presented techniques shown in Table 1, future work will improve and extend deconvolution methods for fMRI. For instance, the appropriate formulation depending on data acquisition (i.e., single-echo vs multi-echo) could be studied and compared with existing methods (Caballero-Gaudes et al. 2019), or formulations that account for HRF variability could be investigated too (Badillo et al. 2013; Gaudes et al. 2012; Farouj et al. 2019). Furthermore, robust methods to select the regularization parameter (Uruñuela et al. 2020; Meinshausen and Bühlmann 2010) and other potential $\ell_{p,q}$ -norm regularization terms (e.g., $p < 1$) or debiasing approaches could be explored.

185

190

Paradigm Free Mapping	Total Activation
+ Its formulation can be extended straightforwardly for deconvolution of multiple signals with a common neuronal-related signal, e.g., for multi-echo formulations Caballero-Gaudes et al. 2019.	+ Both the spike and block models solve the regularization problem with the same HRF.
+ The model can implement any HRF shape very easily since it only requires the coefficients at the required temporal resolution.	-
-	-

Table 1: Advantages (+) and disadvantages (-) of Paradigm Free Mapping and Total Activation with respect to each other.

6. Code availability

²⁰⁰ The code and materials used in this work can be found in the following GitHub repository: https://github.com/eurunuela/pfm_vs_ta. We encourage the reader to explore the parameters (e.g. SNR, varying HRF options and mismatch between algorithms, TR, number of events, onsets, and durations) in the provided Jupyter notebooks.

7. Acknowledgements

²⁰⁵ This research was funded by the European Union's Horizon 2020 research and innovation program (agreement No. 713673 of the Marie Skłodowska-Curie grant), La Caixa Foundation (ID 100010434, fellowship code LCF/BQ/IN17/11620063), the Spanish Ministry of Economy and Competitiveness (RYC-2017-21845), the Basque Government (BERC 2018-2021, PIBA_2019_104, PRE_2019_1_005 4), and the Spanish Ministry of Science, Innovation and Universities (PID2019-
²¹⁰ 105520GB-100).

References

- Allan, T.W., Francis, S.T., Caballero-Gaudes, C., Morris, P.G., Liddle, E.B., Liddle, P.F., Brookes, M.J., Gowland, P.A., 2015. Functional connectivity in mri is driven by spontaneous bold events. *PloS one* 10, e0124577.
- ²¹⁵ Badillo, S., Vincent, T., Ciuciu, P., 2013. Group-level impacts of within-and between-subject hemodynamic variability in fMRI. *Neuroimage* 82, 433–448.
- Beck, A., Teboulle, M., 2009. A fast iterative shrinkage-thresholding algorithm. *Society for Industrial and Applied Mathematics Journal on Imaging Sciences* 2, 183–202. doi:10.1137/080716542.
- ²²⁰ Betzel, R.F., Byrge, L., Esfahlani, F.Z., Kennedy, D.P., 2020. Temporal fluctuations in the brain's modular architecture during movie-watching. *NeuroImage* 213, 116687. doi:10.1016/j.neuroimage.2020.116687.
- Birn, R.M., Diamond, J.B., Smith, M.A., Bandettini, P.A., 2006. Separating respiratory-variation-related fluctuations from neuronal-activity-related fluctuations in fMRI. *Neuroimage* 31, 1536–1548.
- ²²⁵ Bommarito, G., Tarun, A., Farouj, Y., Preti, M.G., Petracca, M., Droby, A., El Mendili, M.M., Inglese, M., Van De Ville, D., 2020. Functional network dynamics in progressive multiple sclerosis. *medRxiv* .
- Bruckstein, A.M., Donoho, D.L., Elad, M., 2009. From Sparse Solutions of Systems of Equations to Sparse Modeling of Signals and Images. *SIAM Review* 51, 34–81. doi:10.1137/060657704.
- ²³⁰ Caballero-Gaudes, C., Moia, S., Panwar, P., Bandettini, P.A., Gonzalez-Castillo, J., 2019. A deconvolution algorithm for multi-echo functional mri: Multi-echo sparse paradigm free mapping. *NeuroImage* 202, 116081.

- Caballero Gaudes, C., Petridou, N., Francis, S.T., Dryden, I.L., Gowland, P.A., 2013. Paradigm free mapping with sparse regression automatically detects single-trial functional magnetic resonance imaging blood oxygenation level dependent responses. *Human Brain Mapping* doi:10.1002/hbm.21452.
- Cherkaoui, H., Moreau, T., Halimi, A., Ciuciu, P., 2019. Sparsity-based Blind Deconvolution of Neural Activation Signal in fMRI, in: ICASSP 2019 - 2019 IEEE International Conference on Acoustics, Speech and Signal Processing (ICASSP), pp. 1323–1327. doi:10.1109/ICASSP.2019.8683358.
- Cifre, I., Flores, M.T.M., Ochab, J.K., Chialvo, D.R., 2020a. Revisiting non-linear functional brain co-activations: directed, dynamic and delayed. *arXiv preprint arXiv:2007.15728*.
- Cifre, I., Zarepour, M., Horovitz, S., Cannas, S., Chialvo, D., 2020b. Further results on why a point process is effective for estimating correlation between brain regions. *Papers in Physics* 12, 120003–120003.
- Cox, R., 1996. AFNI: Software for analysis and visualization of functional magnetic resonance neuroimages. *Computers and Biomedical Research* 29, 162–173.
- Efron, B., Hastie, T., Johnstone, I., Tibshirani, R., 2004. Least Angle Regression. *The Annals of Statistics* 32, 407–499. doi:10.1214/009053604000000067.
- Elad, M., Milanfar, P., Rubinstein, R., 2007. Analysis versus synthesis in signal priors. *Inverse problems* 23, 947.
- Esfahlani, F.Z., Jo, Y., Faskowitz, J., Byrge, L., Kennedy, D.P., Sporns, O., Betzel, R.F., 2020. High-amplitude cofluctuations in cortical activity drive functional connectivity. *Proceedings of the National Academy of Sciences* 117, 28393–28401.
- Farouj, Y., Karahanoğlu, F.I., Van De Ville, D., 2019. Bold signal deconvolution under uncertain haemodynamics: A semi-blind approach, in: 2019 IEEE 16th International Symposium on Biomedical Imaging (ISBI 2019), IEEE. pp. 1792–1796.
- Faskowitz, J., Esfahlani, F.Z., Jo, Y., Sporns, O., Betzel, R.F., 2020. Edge-centric functional network representations of human cerebral cortex reveal overlapping system-level architecture. Technical Report. Nature Publishing Group.
- Faskowitz, J., Tanner, J.C., Mišić, B., Betzel, R.F., 2021. An Edge-Centric Model for Harmonizing Multi-Relational Network Datasets. Preprint. *Neuroscience*. doi:10.1101/2021.01.07.425450.
- Gaudes, C.C., Karahanoğlu, F.I., Lazeyras, F., Van De Ville, D., 2012. Structured sparse deconvolution for paradigm free mapping of functional MRI data, in: 2012 9th IEEE International Symposium on Biomedical Imaging (ISBI), IEEE. pp. 322–325.
- Gaudes, C.C., Petridou, N., Dryden, I.L., Bai, L., Francis, S.T., Gowland, P.A., 2011. Detection and characterization of single-trial fMRI bold responses: Paradigm free mapping. *Human Brain Mapping* doi:10.1002/hbm.21116.
- Gitelman, D.R., Penny, W.D., Ashburner, J., Friston, K.J., 2003. Modeling regional and psychophysiological interactions in fMRI: The importance of hemodynamic deconvolution. *NeuroImage* 19, 200–207. doi:10.1016/S1053-8119(03)00058-2.

- Gonzalez-Castillo, J., Caballero-Gaudes, C., Topolski, N., Handwerker, D.A., Pereira, F., Bandettini, P.A., 2019. Imaging the spontaneous flow of thought: Distinct periods of cognition contribute to dynamic functional connectivity during rest. *NeuroImage* 202, 116129. doi:10.1016/j.neuroimage.2019.116129.
- Jenkinson, M., Beckmann, C.F., Behrens, T.E., Woolrich, M.W., Smith, S.M., 2012. *Fsl. Neuroimage* 62, 782–790.
- Karahanoglu, F.I., Bayram, I., Ville, D.V.D., 2011. A Signal Processing Approach to Generalized 1-D Total Variation. *IEEE Transactions on Signal Processing* 59, 5265–5274. doi:10.1109/TSP.2011.2164399.
- Karahanoglu, F.I., Van De Ville, D., 2015. Transient brain activity disentangles fMRI resting-state dynamics in terms of spatially and temporally overlapping networks. *Nature Communications* 6, 7751. doi:10.1038/ncomms8751.
- Khalidov, I., Fadili, J., Lazeyras, F., Van De Ville, D., Unser, M., 2011. Activelets: Wavelets for sparse representation of hemodynamic responses. *Signal processing* 91, 2810–2821.
- Kinany, N., Pirondini, E., Micera, S., Van De Ville, D., 2020. Dynamic Functional Connectivity of Resting-State Spinal Cord fMRI Reveals Fine-Grained Intrinsic Architecture. *Neuron* 108, 424–435.e4. doi:10.1016/j.neuron.2020.07.024.
- Liu, X., Chang, C., Duyn, J.H., 2013. Decomposition of spontaneous brain activity into distinct fMRI co-activation patterns. *Frontiers in systems neuroscience* 7, 101.
- Liu, X., Duyn, J.H., 2013. Time-varying functional network information extracted from brief instances of spontaneous brain activity. *Proceedings of the National Academy of Sciences* 110, 4392–4397.
- Liu, X., Zhang, N., Chang, C., Duyn, J.H., 2018. Co-activation patterns in resting-state fMRI signals. *Neuroimage* 180, 485–494.
- Lopes, R., Lina, J.M., Fahoum, F., Gotman, J., 2012. Detection of epileptic activity in fMRI without recording the eeg. *Neuroimage* 60, 1867–1879.
- Majeed, W., Magnuson, M., Hasenkamp, W., Schwab, H., Schumacher, E.H., Barsalou, L., Keilholz, S.D., 2011. Spatiotemporal dynamics of low frequency bold fluctuations in rats and humans. *Neuroimage* 54, 1140–1150.
- Majeed, W., Magnuson, M., Keilholz, S.D., 2009. Spatiotemporal dynamics of low frequency fluctuations in bold fMRI of the rat. *Journal of Magnetic Resonance Imaging: An Official Journal of the International Society for Magnetic Resonance in Medicine* 30, 384–393.
- Meinshausen, N., Bühlmann, P., 2010. Stability selection. *Journal of the Royal Statistical Society: Series B (Statistical Methodology)* 72, 417–473.
- Raguet, H., Fadili, J., Peyré, G., 2013. A Generalized Forward-Backward Splitting. *SIAM Journal on Imaging Sciences* 6, 1199–1226. doi:10.1137/120872802.
- Schwarz, G., 1978. Estimating the Dimension of a Model. *Annals of Statistics* 6, 461–464. doi:10.1214/aos/1176344136.

- ³¹⁰ Shine, J.M., Bissett, P.G., Bell, P.T., Koyejo, O., Balsters, J.H., Gorgolewski, K.J., Moodie, C.A., Poldrack, R.A., 2016. The dynamics of functional brain networks: integrated network states during cognitive task performance. *Neuron* 92, 544–554.
- ³¹⁵ Shine, J.M., Koyejo, O., Bell, P.T., Gorgolewski, K.J., Gilat, M., Poldrack, R.A., 2015. Estimation of dynamic functional connectivity using multiplication of temporal derivatives. *NeuroImage* 122, 399–407.
- Shmueli, K., van Gelderen, P., de Zwart, J.A., Horovitz, S.G., Fukunaga, M., Jansma, J.M., Duyn, J.H., 2007. Low-frequency fluctuations in the cardiac rate as a source of variance in the resting-state fMRI bold signal. *Neuroimage* 38, 306–320.
- ³²⁰ Tarun, A., Wainstein-Andriano, D., Sterpenich, V., Bayer, L., Perogamvros, L., Solms, M., Axmacher, N., Schwartz, S., Van De Ville, D., 2020. Nrem sleep stages specifically alter dynamical integration of large-scale brain networks. *Iscience* 24, 101923.
- Tibshirani, R., 1996. Regression Shrinkage and Selection Via the Lasso. *Journal of the Royal Statistical Society: Series B (Methodological)* 58, 267–288. doi:10.1111/j.2517-6161.1996.tb02080.x.
- ³²⁵ Triantafyllou, C., Hoge, R.D., Krueger, G., Wiggins, C.J., Potthast, A., Wiggins, G.C., Wald, L.L., 2005. Comparison of physiological noise at 1.5 t, 3 t and 7 t and optimization of fMRI acquisition parameters. *Neuroimage* 26, 243–250.
- ³³⁰ Uruñuela, E., Jones, S., Crawford, A., Shin, W., Oh, S., Lowe, M., Caballero-Gaudes, C., 2020. Stability-Based Sparse Paradigm Free Mapping Algorithm for Deconvolution of Functional MRI Data. *Proceedings of the Annual International Conference of the IEEE Engineering in Medicine and Biology Society*, EMBS 2020-July, 1092–1095. doi:10.1109/EMBC44109.2020.9176137.
- Zhang, X., Pan, W.J., Keilholz, S.D., 2020. The relationship between bold and neural activity arises from temporally sparse events. *Neuroimage* 207, 116390.
- ³³⁵ Zöller, D., Sandini, C., Karahanoğlu, F.I., Padula, M.C., Schaer, M., Eliez, S., Van De Ville, D., 2019. Large-scale brain network dynamics provide a measure of psychosis and anxiety in 22q11.2 deletion syndrome. *Biological Psychiatry: Cognitive Neuroscience and Neuroimaging* 4, 881–892.

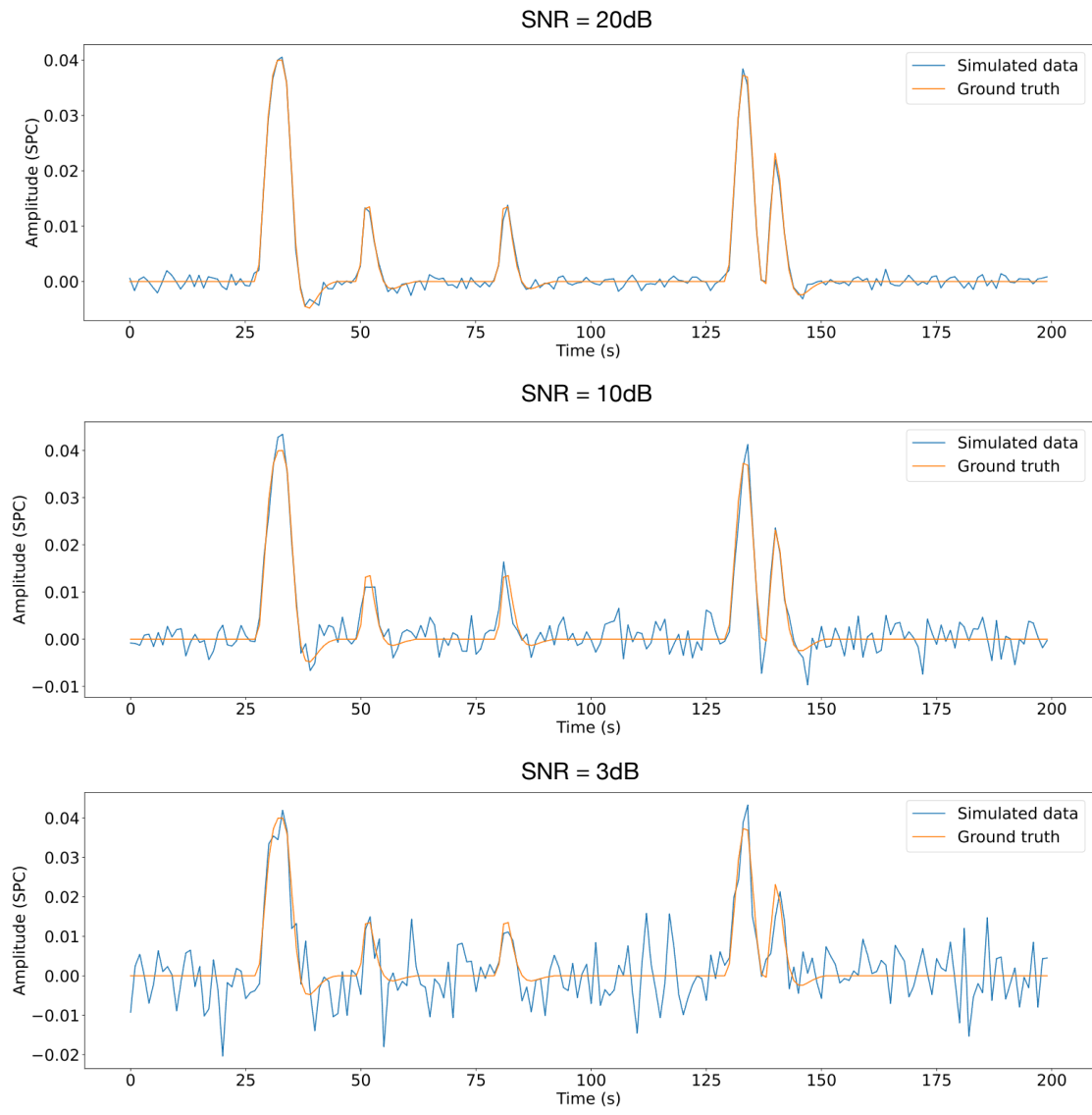


Figure 1: Simulated signal with different SNRs (20 dB, 10 dB and 3 dB).

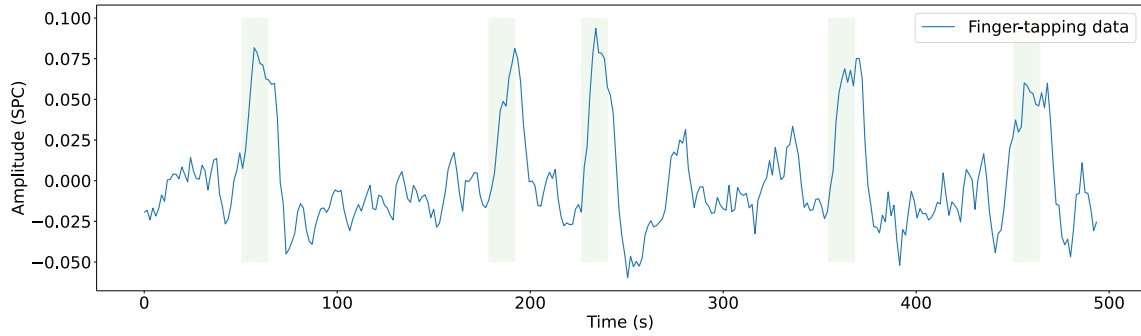


Figure 2: Most representative voxel of the finger-tapping task. Green blocks indicate the onsets and the duration of it.

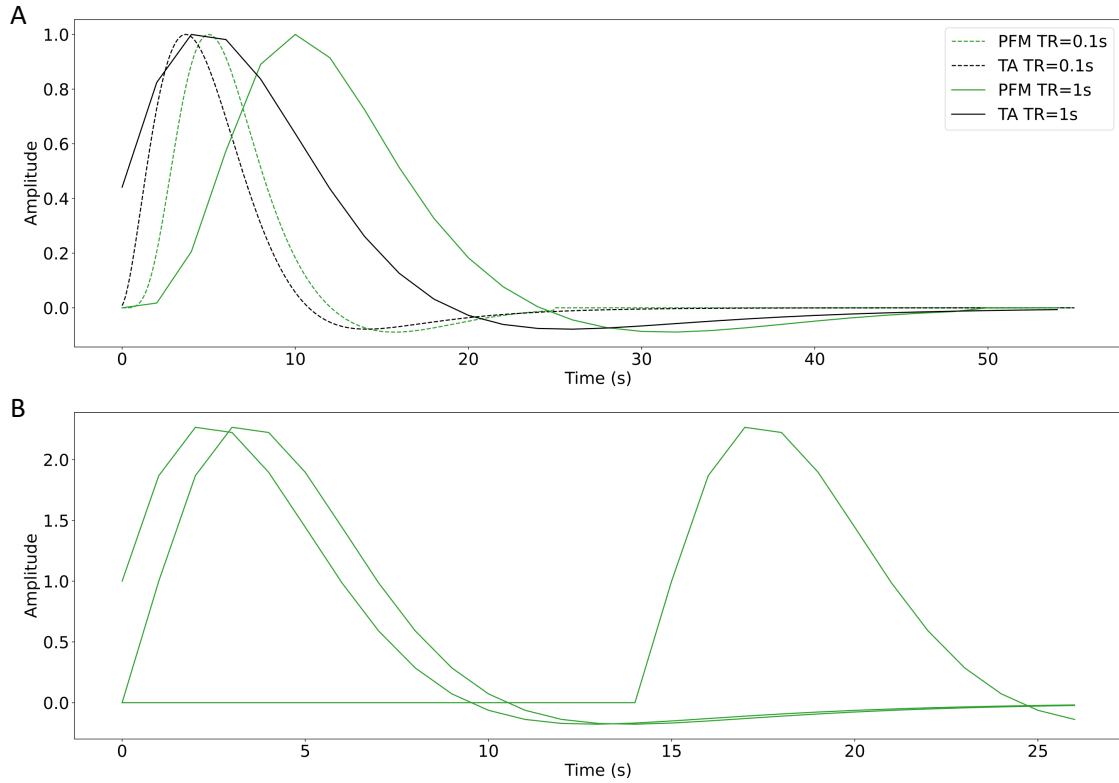


Figure 3: A) Canonical HRF models typically used by PFM (green) and TA (black) at TR = 0.1 s (dashed lines) and TR = 1 s (solid lines). Without loss of generality, the waveforms are scaled to unit amplitude for visualization. B) Representation of three shifted HRFs at TR=1 s (onsets=0, 1, and 15 s) that build the design matrix for PFM when the HRF model has been matched to that in TA.

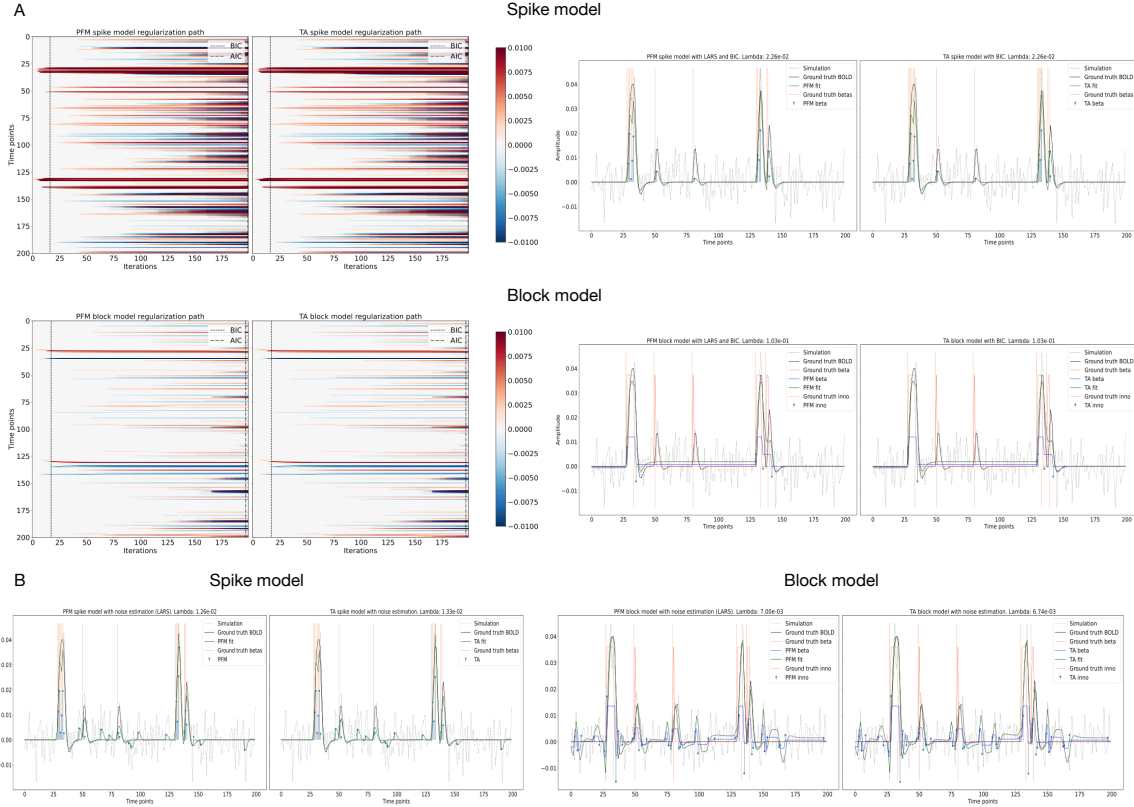


Figure 4: A) (Left) Heatmap of the regularization paths of the activity-inducing (top) and innovation (bottom) signals estimated with PFM and TA as a function of λ for the simulated data with SNR = 3 dB (x-axis: increasing number of iterations or λ as given by LARS; y-axis: time; color: amplitude). Vertical lines denote iterations corresponding to the Akaike and Bayesian Information Criteria (AIC and BIC) optima. (Right) Estimated activity-inducing (blue) and activity-related (green) signals λ is selected based on BIC. B) Estimated activity-inducing, innovation and activity-related (fit, \mathbf{x}) signals when λ is selected based on the MAD method with the spike model (left, with PFM on the left and TA on the right) and block model (right, with PFM on the left and TA on the right) for the simulated data with SNR = 3 dB.

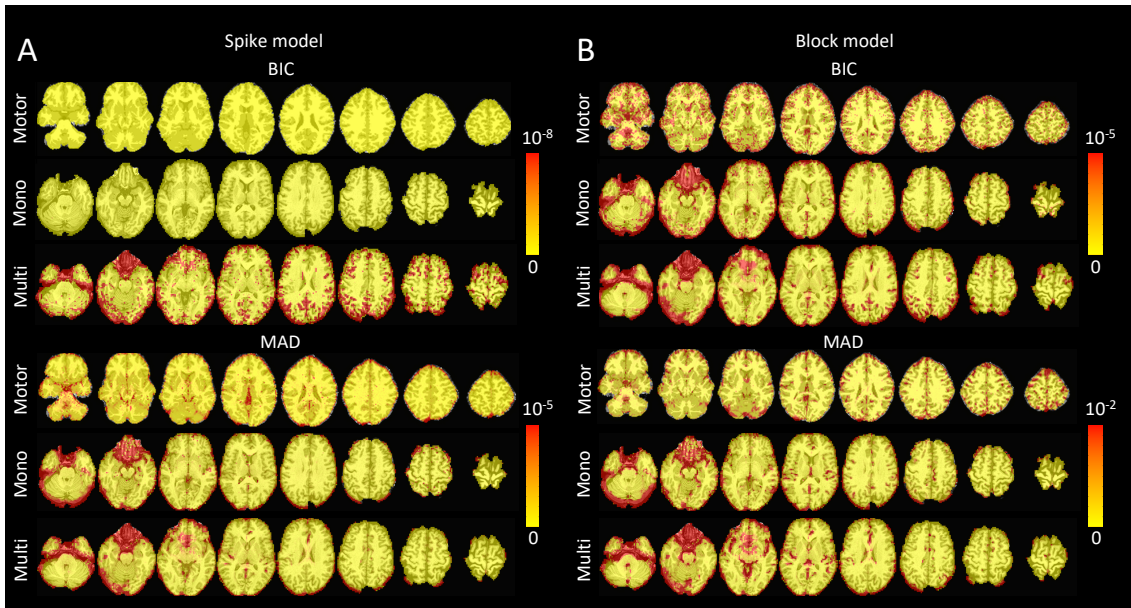


Figure 5: Sum of squares of the differences of the activity-inducing signals estimated with Paradigm Free Mapping and Total activation for the different selections of the regularization parameter: BIC (top), and MAD (bottom). The sum of square difference maps are shown for the three experimental datasets introduced in Section 3: the motor task (Motor), the monoband resting-state (Mono), and the multiband resting-state (Multi) datasets. A) Sum of squares of the differences when using the spike model. B) Sum of squares of the differences when using the block model.

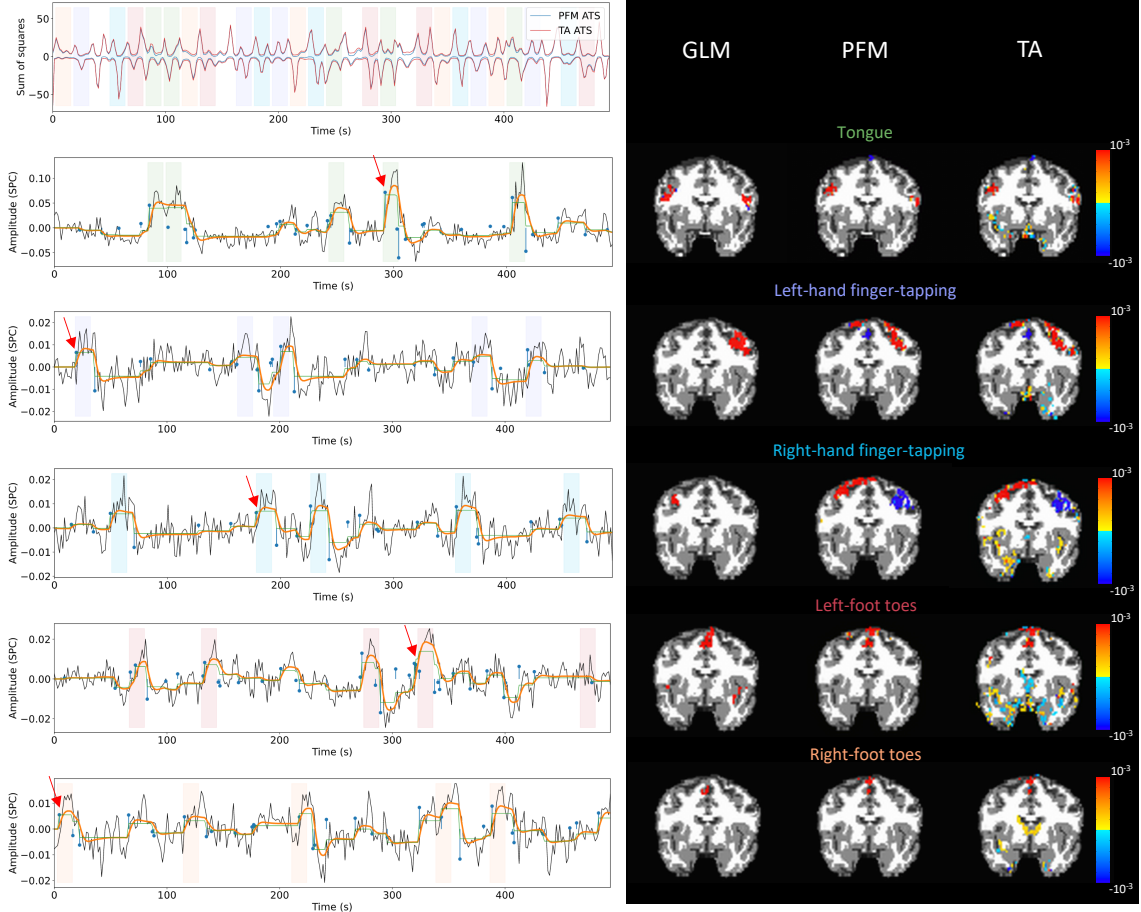


Figure 6: Row 1: Activation time-series of the innovation signals estimated by PFM calculated as the sum of squares at every time-frame. Color-bands indicate the onset and duration of each condition in the task (green: tongue, purple: left-hand finger-tapping, blue: right-hand finger-tapping, red: left-foot toes, orange: right-foot toes). Rows 2-6: time-series of a representative voxel for each task with the PFM-estimated innovation (blue) and neuronal-related (i.e., fitted, orange) signals, with their corresponding GLM, PFM and TA maps on the right.

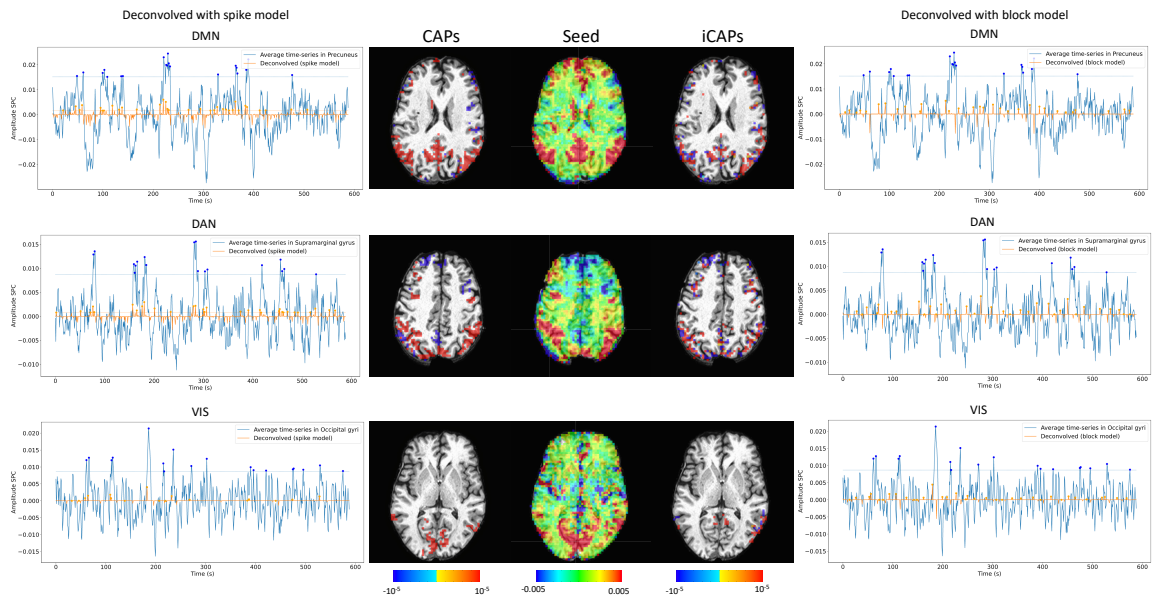


Figure 7: CAPs (left) and iCAPs (right) obtained with the PFM-estimated activity-inducing and innovation signals respectively. Time-points selected with a 95th percentile threshold are shown over the average time-series (blue) in the seed region (white-cross) and the deconvolved signal (orange). CAPs and iCAPs maps of the seed and deconvolved signals obtained by averaging the selected time-points are illustrated in the center.